IMPROVED PORE NETWORK EXTRACTION METHODS

A.P. Sheppard, R. M. Sok and H. Averdunk
Mesoscale Physics Group, Applied Mathematics, ANU

This paper was prepared for presentation at the International Symposium of the Society of Core Analysts held in Toronto, 21-25 August 2005

ABSTRACT

Pore network models, in which the pore space is represented by a 3D network of interconnected pores and throats, are used extensively to compute important macroscopic transport properties including capillary pressure, relative permeability and residual saturation [2,6,12]. The predictive value of network models depends on the accuracy with which the network captures the complex geometric and topological properties of real porous rocks. A practical approach for a wide range of rock types is to extract networks and network properties directly from high-resolution 3D images of the pore space [2,7,8]. To ensure that generated networks are accurate representations of the imaged rock one must overcome problems of sensitivity to image noise and the lack of a robust procedure for merging adjacent nodes to form pores. One must also be able to generate networks on 3D volumes that are sufficiently large to be representative .

We present an evolutionary approach for network extraction that uses the medial axis transform together with a number of morphological measures to select tessellation boundaries and applies a new node merging algorithm. The algorithms are fully parallel, allowing very large networks containing up to a million nodes to be generated. The power and flexibility of the network extraction procedure is illustrated by examining micro-CT images for a number of sandstone and carbonate samples at image sizes of up to 2000^3 voxels and resolutions down to 2 microns. The variability in network structure obtained across the range of samples imaged highlights the need to generate realistic pore network structures when attempting to perform predictive two phase flow modeling.

INTRODUCTION

There are several reasons why a core analyst would want to generate a network of pores and throats that is representative of the pore space of a reservoir rock. For one, the pore throat network contains a wealth of geometrical and topological information that can be invaluable in characterising the morphological structure of the pore space. However, the main reason for generating pore networks is that they are the input to network models, which remain the most promising method for modelling multi-phase fluid displacements[1].

The advent of X-ray micro-tomography has enabled the pore space of reservoir rocks to be imaged. Images containing 2000^3, or 8 billion voxels, are routinely generated and

phase contrast imaging enables resolutions of 300nm or better [2, 3]. In parallel with these experimental advances, a number of research groups have developed methods to generate pore-networks that capture the pore space of imaged rocks[4-8].

The problem of network generation is essentially one of partitioning the pore space into simple building blocks, or components. Adjacent components are connected by links, forming a network. There are two main schools of thought as to how best identify these building blocks. The first [4,5] uses the medial axis transform to reduce the pore space to its 1D line skeleton. The junctions in the skeleton then form the basis for pore bodies, while the chains of voxels connecting them are identified with pore throats. One must then process the skeleton, primarily by merging junctions that are in close proximity, to generate the pore network. Fundamental to the medial axis approach is the assumption that the pore network is first and foremost a topological representation of the pore space.

The other school of thought [6] takes issue with this assumption, and instead relies solely on the tools of mathematical morphology to arrive at a partitioning of the pore space. In this paradigm, the pore network is primarily a geometrical concept. This rationale can easily be justified since pure capillary-driven fluid displacement is a geometrical process; indeed mercury porosimetry can be very effectively simulated directly on a binarised image, using little more than the basic tools of mathematical morphology[9]. In addition, one can easily postulate scenarios in which junctions in the medial axis simply do not correspond to geometric openings, and vice versa.

However, there are a number of serious shortcomings to the geometrical approach. First is the sensitivity to noise. It is easy to see that small perturbations to the surface of the grain space can lead to large variations in the resultant network. When applying a purely morphological model to a real rock image, one is forced to post-process the carefully derived network by an additional merging step, thus losing much of the intuitive appeal of this method [6]. The second drawback of the geometric approach is that there is no longer a defined relationship between the topology of the pore network and that of the original pore space. A great many geometrical features produce loops in the resulting network that were not present in the original pore space, while, on the other hand, there is no guarantee that pore bodies will be simply connected. These two shortcomings exacerbate each other's effects to the extent that a network based on geometry alone must be treated with caution.

In this work we try to capture the best of both worlds. We insist on building blocks that are simply connected, and on generating a network that is homeomorphic to the original pore space. We therefore base our network structure on the medial axis, and also use a broad range of tools from mathematical morphology to best capture the pore-space geometry within the topological constraints.

ALGORITHM

Beginning with a reconstructed, grey-scale tomographic image, our method proceeds in multiple steps. All the steps outlined here are performed by the in-house "mango"

parallel toolkit for morphological analysis and network generation and have been performed on images containing up to 2000^3 voxels.

Image Processing And Segmentation

As explained in [10], we apply anisotropic diffusion for edge-preserving noise reduction, followed by the unsharp mask filter for edge enhancement. After this, high contrast data sets can be segmented using simple thresholding, while more complex samples mandate use of the method of *converging active contours*.

Medial Axis Transform

To minimise ordering effects and ensure that the medial axis is as close to the geometric centre as possible, we calculate the medial axis using distance ordered homotopic thinning [11]. Voxels are treated in order of their Euclidean distance values, and are removed only if their removal does not change the homotopy (or, equivalently, the Betti numbers) of the pore space. We have found that by applying a Gaussian smoothing kernel to the Euclidean distance map, and using this as the ordering function for the thinning algorithm, that the resultant medial axis contains fewer spurious features. We have also found it better to perform the first few steps of the homotopic thinning assuming that the object being thinned is 6-connected, before switching to 26-connectivity for the remainder of the process. This eliminates connections being formed across voxel corners or edges, while still allowing the final medial axis to have 26-connectivity.

This algorithm has been parallelised using a time warp optimistic parallel discrete event simulator, and it has been run on hundreds of cpus routinely, finding the medial axis of samples containing up to 8 billion voxels.

Network Connectivity

The topology of our medial axis based pore network is completely defined by the pore space. On the other hand, the connectivity of this network is non-unique and can vary enormously. This is because one can merge or divide nodes of the network without changing the topology of the network. Any operation that does not collapse an existing ring, or create a new ring, is allowed. In addition, one can also add or remove any number of two-connected nodes within throats/links/edges.

We construct a starting network by dividing the medial axis into clusters of voxels that are (26-) adjacent to more than 2 other medial axis voxels, and chains of voxels that connect just two other medial axis voxels. Since this starting network will be composed almost entirely of 3-connected nodes which represent only parts of pore bodies, merging is of critical importance to a medial axis derived network.

Previous merging algorithms seem to have neglected two important issues: topology preservation and snowballing. When merging pores, one must be careful not to merge

two pores that are already connected to one another by more than one throat. If this occurs, then the non-collapsed throat becomes a loop that connects the merged pore body to itself, which can therefore play no role in the transport. This altering of the network topology is clearly undesirable behaviour and is forbidden in our algorithm. Snowballing occurs when one merges pores using the purely local criteria proposed previously. Figure 1 shows a type of geometry in which undesirable pore merging can occur. To a local analysis, each pair of pores seems to be a good candidate for merging; it is only when one stands back and observes the newly merged pore in its entirety that the folly is exposed. While this may appear to be a singular pathological example, our experience shows that, in fact, the majority of pore bodies are "pathological" in one way or another.

To address these issues, our merging algorithm operates as follows:

1. The quality of each throat is calculated as a nonlinear combination of its *constriction ratio* and *length-width ratio*. The constriction ratio measures the ratio between the smaller of the two maximal radii in the adjoining pore bodies adjoining the throat, and the smallest radius in the throat. The length-width ratio measures the ratio between the throat length, defined as the straight-line distance between the pore centres, and the minimum throat width. These measures are combined in such a way that very short throats always have extremely low quality, while very constrictive throats always a high quality. Throats whose quality is below a certain threshold are candidates for removal.

2. The throats that are candidates for removal are stored in a list, sorted from lowest to highest quality, from which the lowest quality throat is extracted for treatment at each step. If removal of a throat doesn't change the network topology, then it is removed. In that case, the newly formed pore will have a new centre of geometry, and is maximal radius will come from the larger of its two constituent pores. The new centre and radius is therefore used to update the quality of any low-quality throats connected to the new pore. Normally the change will increase the quality of the throats, thereby reducing their likelihood of being merged.

3. The algorithm terminates when there are no more low quality throats that can be removed without changing the network topology.

It should be emphasised that without dynamic updates of throat qualities during the merging process, it is not possible to avoid snowballing.

Geometric Partitioning

Having determined the connectivity, i.e. identified all the pore bodies and throats in the network, it remains to determine the geometry of these components, which means that one must partition the pore space. Whether one needs to partition the pore space into pore bodies *and* pore throats, or just into pore bodies, is an issue of some controversy in the network modelling literature. Some network models appear to need some volume allocated to throats [1,12] in order to match experimentally observed residual saturations, while other models [13] perform adequately without this additional complexity. Our algorithm first partitions the pore space into pore bodies alone, then takes volume from

the pore bodies to form pore throats. We can therefore easily generate networks for either type of network model.

First, we partition the pore space into pore bodies, without allocating any volume to throats: in this model, a throat is just the surface where the regions surrounding two adjacent pores touch. This partitioning is achieved using the watershed transformation[9] applied to the (smoothed) Euclidean distance map, initialised with seed regions formed from the medial axis voxels associated with each pore body. The watershed transform expands from the seed voxels, processing neighbouring voxels in order from highest to lowest Euclidean distance, and assigning them to the same cluster as their highest-valued neighbour. The watershed surface of the distance transform forms a good definition of the minimum throat constriction.

Next we take each of these pore bodies and allocate some of its volume to the pore throats that connect to it. Our definition of pore bodies and throats simulates the following experiment: fill the pore body with wetting phase, then fill the maximal euclidean sphere of the pore body with non-wetting phase. This configuration is the lowest capillary pressure at which the non-wetting phase can be present in the pore body. Then, successively increment the capillary pressure, which decreases the hydraulic radius, enabling the region of non-wetting phase to expand into smaller and smaller constrictions. Eventually, the wetting-phase in one of the throats that adjoin the pore body will be disconnected from the other throats. The growth into that throat stops, and the boundary between the pore and the throat is defined. The growth continues until all the throats have been disconnected from one another.

Analysis of the profile of each throat (akin to [5]) can be used to decide whether or not the throat contains more than one genuine constriction, in which case it is divided and a pore body, perhaps more than one, is inserted. This processing step has not been applied to the networks presented in this study. We will include this in future work.

DATA SETS

This study is based on four datasets. We have taken 600^3 subsets from four 2000^3 tomographic images captured using the ANU high-resolution CT facility[2]. Slices from these images are shown in figure 2. Armed with fully parallel algorithms, we have the capacity to study the full 2000^3 data sets, but here we present preliminary results.

Due to the finite resolution and inaccuracies in the reconstruction process, there is an uncertainty in the segmentation step. To estimate the sensitivity of subsequent analysis to the variation of segmentation parameters, we perfomed three different segmentations on two of the data sets: one with porosity near the lower limit of acceptability (“low”), another near the top limit (“high”), and one in the middle(“mid”). Table 1 shows the porosity of these three data sets before and after removal of isolated clusters. Only the poorly connected data set B shows a significant disconnected fraction. Table 1. also shows the critical radius[14] of these data sets, calculated by percolation on the medial axis.

To further explore the parameter space, we generate 3 different networks for a number of the "mid" segmented images that we have already obtained. These networks differ in the amount of pore merging that is performed. As with the different segmentations, these "merge" and "nomerge" data sets lie near the reasonable limits of the parameter space. Note that the topology (genus) of all the networks arising from the same segmented image is the same, but the connectivity and the number of pores and throats is different.

RESULTS

Table 1 summarises the results of this work. l_{vox} is the voxel size, in µm. The instrument resolution is around 2µm, so these runs are near but not at the limit of the facility. φ and φ_{IC} are the porosity before and after the removal of isolated clusters. it can be seen that none of the samples have a great deal of disconnected pore space, although the disconnected fraction was up to 10% of the porosity for lower porosity samples. l_c is the critical radius of the pore space, defined as the largest sphere that can be pushed through the pore space from one of the sample side to the other. The critical length is a surprisingly good predictor of permeability [14]. N_p and N_t are the number of pores and throats in the generated networks, while $N_{p(red)}$ and $N_{t(red)}$ show the proportion of pores and of throats that were lost in the pore merging process. G/mm^3 is the genus, or the number of handles, calculated as the difference between the number of throats and the number of pores, expressed per unit volume; $<z>$ is the average coordination number of the pores in the generated network, while z_{max} is the maximum coordination number; $<RS>$ represents the mean ring size. Rings, or minimal circuits, are defined to be strong rings [14]. Interestingly, the average ring size does not vary greatly between the samples, although the ring size distributions, which we do not present, show significant variation. $<r_p>$ and $<r_t>$ are the average pore and throat radius respectively. It is worth noting that the average throat radius, and the critical length l_c are only a few voxels, indicating that for the sandstone samples, there is a lot of important feature at or near the limit of resolution. On the other hand, the highly permeable limestone has a much larger critical length, meaning that its plethora of small throats play little part in the permeability. $<l_t>$ is the average throat length, measured as the distance between the pore centres, while $<r_p/r_t>$ is the average constriction ratio, or the ratio between a pore's radius and the radius of the throats surrounding it. $p_c(s)$ and $p_c(b)$ are the site and bond percolation thresholds of the network. These are the fraction of sites (pores) or bonds (throats) that need to be filled in order that a cluster of filled elements connects across the sample. We have calculated these thresholds since percolation processes capture much of the dynamics of multiphase flow.

The networks appear to be rather robust to both the segmentation parameters and to the criteria used in the merging of overlapping pore bodies. The samples segmented at higher porosities are better connected, and show higher coordination numbers and marginally bigger pore and throat sizes. The networks produced by varying pore merging criteria show significant but not unexpected variation in all parameters. In these data

sets, there is no evidence of instability or nonlinear sensitivity to these parameters: small changes in the input data result in small changes to the resultant networks.

The most striking result of this study lies in the connectivity of the pore networks, particularly of the two sandstones, and the consequences that this has for the percolation threshold. Figure 2 shows the obtained networks, which are very different from one another in appearance and measures, despite appearing to be similar in two-dimensional slices. The sandstone-1 network is of particular interest in that despite having an average coordination number of only 4.3, it has very many 3-rings. This is perhaps an explanation for its rather high percolation threshold of 0.50. Indeed, the large variation in the percolation threshold between the networks, despite having reasonably similar coordination numbers, shows that these rocks possess very interesting topological structure.

To understand better the prevalence of 3-rings in the sandstone-1 sample, we took a very small subset containing a 3-ring and present it in figure 3. This subset is fascinating in that it is not immediately apparent how best to represent it as a network. The main feature is a large donut shaped element with a reasonably small hole in the middle - very much what one would expect from two touching grains. Our topological merging criteria forbids us from merging it, so our network forms a 3-ring around the donut. It is clear that this feature represents a genuine 3-ring that is not an artefact of the network extraction. Given that this type of feature is visible throughout the data set, we conclude that 3-rings are a real feature.

CONCLUSIONS AND FURTHER WORK

This preliminary study raises more questions than it answers, and we do not yet have a coherent understanding of the structural characteristics that underlie the results that we present here. We can, however, draw some concrete conclusions. Firstly, the network generation method is robust to variation in the parameters that govern both image segmentation and pore merging. This is very encouraging. It is also very encouraging that, despite the great variability in the networks and rock types considered, that the vast majoriy of throats in the generated networks represent genuine constrictions to flow.

We have also demonstrated that use of the non-local pore merging algorithms, such as the one that we introduce here, is critical for achieving representative networks.

Future work will initially focus on further validation of our network extraction algorithm. We are in the process of developing measures to better quantify how well a network represents the pore space. By examining a large selection from the wide range of rock samples that have been imaged in our department, we hope to build up a coherent picture of the interrelationships between these measures.

It is also of critical importance to directly compare our networks with those generated using other means. To this end, we aim to share our data and results with other groups conducting similar research.

REFERENCES

1. Blunt, M. J. "Flow in porous media - pore-network models and multiphase flow", Curr. Opin. Colloid Interface Sci. (2001), 63, 197-207
2. Sakellariou, A., T. J. Sawkins, T. J. Senden and A. Limaye, "X-ray tomography for mesoscale physics applications", Physica A, (2004), 339, 152-158
3. http://www.esrf.fr/UsersAndScience/Experiments/Imaging/ID19
4. Lindquist, W. B., S.-M. Lee, D.A. Coker, J.W. Jones, and P. Spanne, "Medial Axis Analysis of Void Structure in Three-Dimensional Tomographic Images of Porous Media", J. Geophys. Res. 101B, (1996) 8297-8310.
5. Liang, Z., M. A. Ioannidis and I. Chatzis, Geometric and topological analysis of three-dimensional porous media: pore space partitioning based on morphological skeletonisation , J. Colloid Interface Sci. (2000) 221, 13-24
6. Silin, D, B. and T. W. Patzek, Robust determination of the pore space morphology in sedimentary rocks , Soc. Petrol. Eng. J. (2003), 84296
7. Adler, P. M., C. G. Jacquin and J. A. Quibler , Flow in simulated porous media , Int. J. Multiphase Flow (1990) 16, 691
8. Al-Raoush, R. I. and C. S. Willson Extraction of physically realistic pore network properties from three-dimensional synchrotron X-ray microtomography images of unconsolidated porous media systems , J. Hydrology ,(2005) 300, 44-64
9. Soille, P, "Morphological Image Analysis: Principles and Applications", Springer-Verlag, Berlin (2003)
10. Sheppard, A. P., R. M. Sok and H. Averdunk, "Techniques for image enhancement and segmentation of tomographic images of porous materials", Physica A, (2004) 339, 145-151
11. Pudney C., "Distance-Ordered Homotopic Thinning: A Skeletonization Algorithm for 3D Digital Images", Computer Vision and Image Understanding, (1998) 72, 404-413
12. Oren, P. E. and S. Bakke, "Reconstruction of Berea sandstone and pore-scale modelling of wettability effects", J. Pet. Sci. Eng. (2003), 39, 177-199
13. Chang, D. and Ioannidis, M. A. "Magnetization Evolution in Network Models of Porous Rock under Conditions of Drainage and Imbibition", J. Colloid Interface Sci., vol. 253, p. 159, 200
13. Bauget, F., C. H. Arns, M. Saadatfar, M. L. Turner, A. P. Sheppard, R. M. Sok, W. V. Pinczewski and M. A. Knackstedt, "Rock typing and petrophysical property estimation via direct analysis on microtomographic images, 19th International Symposium of the Society of Core Analysts, Toronto, August 21-25 (2005)
14. O'Keeffe, M. and Hyde, B. G. "Crystal Structures I: Patterns and Symmetry",Mineral. Soc. Am., Washington, D.C., (1996)
15. Arns, J-Y., V. Robins, A. P. Sheppard, R. M. Sok, W. V. Pinczewski and M. A. Knackstedt, "Effect of network topology on relative permeability", Transp. Porous Media, 55, (2004), 21-46

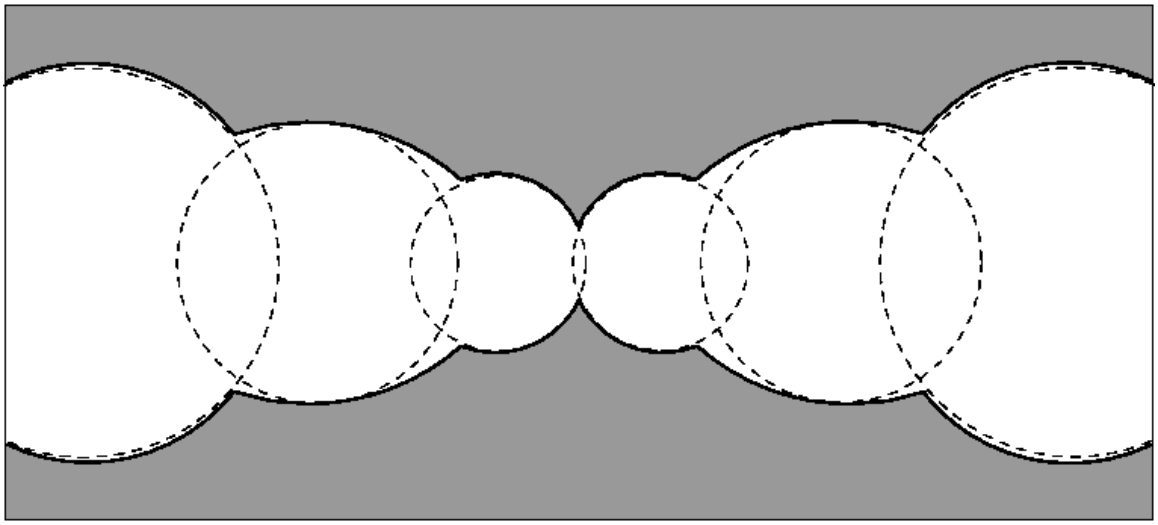

Figure 1. Cross section through a geometry that will be mishandled by local pore merging rules. This whole object, being composed of overlapping maximal spheres, will be merged into a single pore unless a more sophisticated approach, such as that presented here, is used.

	Sandstone-1					Sandstone-2			Limestone	
	High	Low	Mid	Merge	NoMrg	Mid	Merge	NoMrg	Low	Mid
l_{vox}	4.38	¬	¬	¬	¬	5.6	¬	¬	3.0	
φ	18.4%	18.4%	18.4%	¬	¬	25.2%	¬	¬	42.5%	46.9%
φ_{IC}	18.3%	14.7%	16.7%	¬	¬	25.1%	¬	¬	41.1%	46.1%
l_c	10.5	7.4	9.2	¬	¬	11.8	¬	¬	27	28.5
N_p	8407	6921	7876	7218	8915	17160	15094	20853	9362	10408
$N_{p(red)}$	44%	40%	42%	47%	34%	48%	54%	22%	46%	48%
N_t	17997	14267	16593	15935	17632	41389	39323	45082	20713	45082
$N_{t\text{-}(red)}$	27%	26%	26%	29%	22%	28%	32%	22%	29%	29%
G/mm^3	529	405	480	480	480	639	639	639	1947	2305
$<z>$	4.3	4.1	4.2	4.4	4.0	4.8	5.2	4.3	4.4	4.6
z_{max}	26	23	29	29	18	30	29	24	67	80
$<RS>$	5.8	5.9	5.9	5.7	6.1	5.7	5.5	6.0	5.1	5.2
$<r_p>$	21	21	21	21	21	25	26	25	19	20
$<r_t>$	10	9	9.5	9.3	10	12	11	12	8.7	9.3
$<l_t>$	110	120	110	120	100	130	140	120	82	83
$<r_p/r_t>$	2.9	3.0	3.0	3.1	2.8	2.7	2.8	2.5	4.1	4.2
$p_c(s)$	0.46	0.49	0.47	0.45	0.50	0.37	0.35	0.39	0.42	0.39
$p_c(b)$	0.35	0.38	0.36	0.33	0.41	0.28	0.24	0.28	0.27	0.25

Table 1. Summary of the statistics gathered from the pore-networks generated from the 3 rock samples studied in this work. See the text for an explanation of the symbols used in this table.

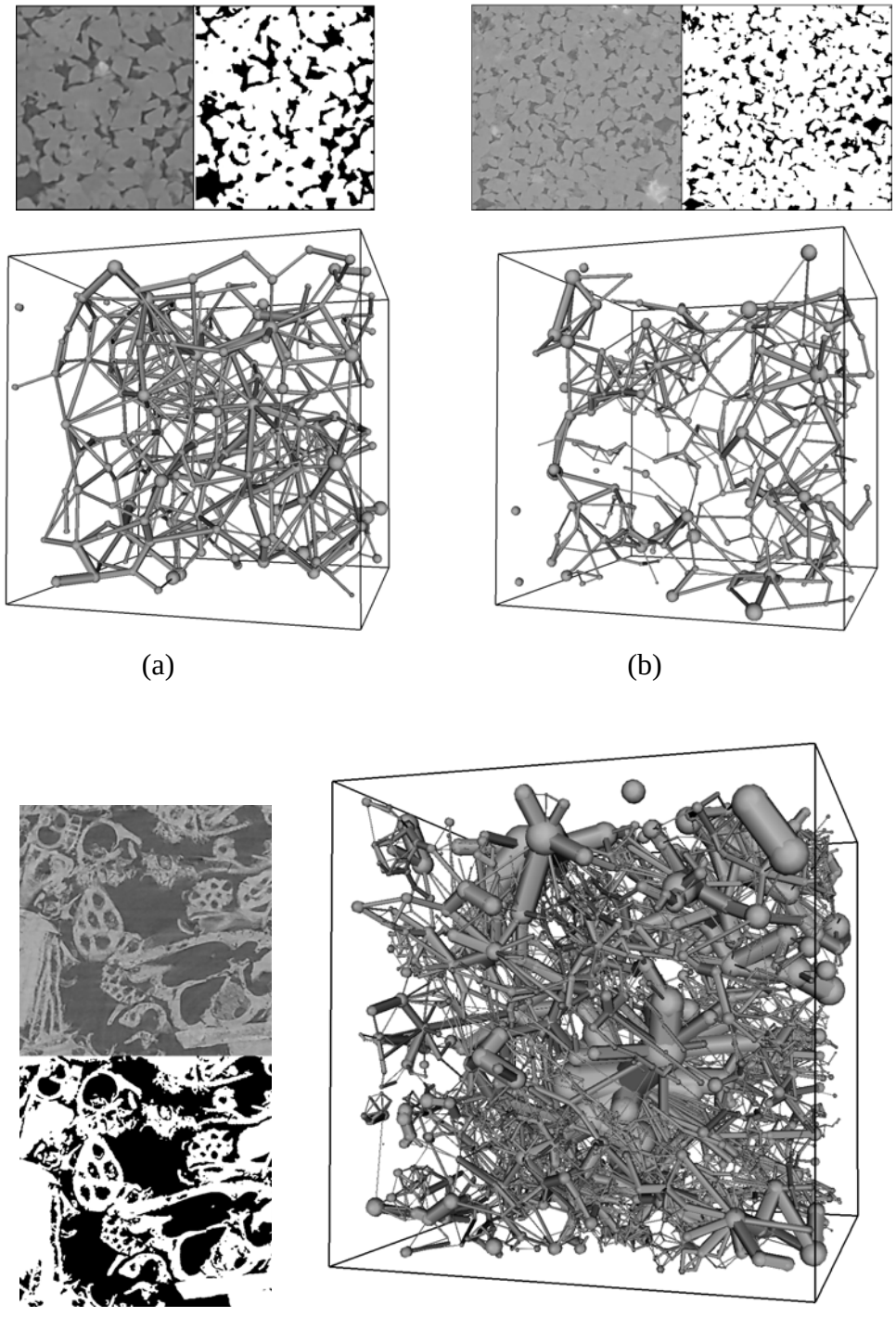

Figure 2. Images of grey-scale and segmented images, shown adjacent to networks for the 3 rock types studied. (a) sandstone-1; (b) sandstone-2; (c) limestone. 200 pore bodies (nodes) are shown in (a) and (b), while 2000 are shown in (c).

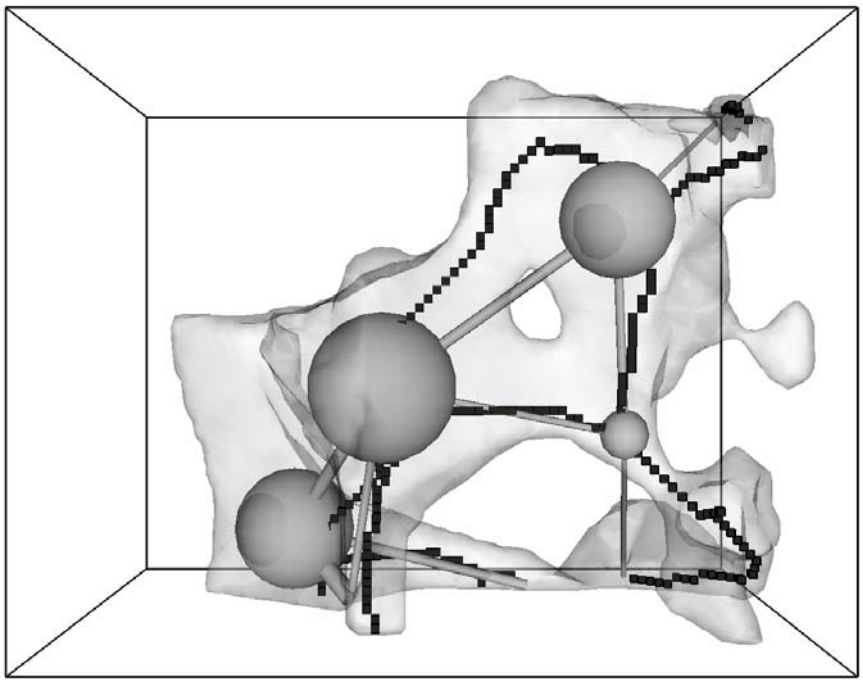

Figure 3. Medial axis and pore network overlaid on a portion of the sandstone-1 dataset, illustrative of a geometry and topology that is difficult to express as a network. Throats are 25% of their true radius.